Computers and Structures 89 (2011) 2522–2530

Contents lists available at ScienceDirect

Computers and Structures

journal homepage: www.elsevier.com/locate/compstruc

Harmonic response computation of viscoelastic multilayered structures using a ZPST shell element

Jean-Daniel Chazot [a,*], Benoit Nennig [a,b], Ameur Chettah [a,c]

[a] Université de Technologie de Compiègne, Laboratoire Roberval UMR 6253, BP 20529, 60205 Compiègne cedex, France
[b] LAUM, UMR6613 CNRS, Université du Maine, Ave. Olivier Messiaen, F-72085 Le Mans cedex 9, France
[c] BATir, ULB, 87 Avenue Buyl, B-1050 Bruxelles, Belgium

ARTICLE INFO

Article history:
Received 21 December 2010
Accepted 19 May 2011
Available online 28 June 2011

Keywords:
Shell element
Multilayer
ZPST
Zigzag
Viscoelastic
Padé approximant

ABSTRACT

This paper uses the ZPST multilayered shell element developed by Sulmoni et al. to compute the dynamic response of multilayered viscoelastic structures such as windscreens or car bodyworks. It is based on the P-order shear deformation theory with an added zigzag function. The viscoelastic properties are taken into account with frequency dependent elastic moduli measured with a Dynamic Mechanical Thermal Analyzer. A method based on Padé approximant is also used to reduce the computation time. This acceleration technique enables to achieve fast frequency sweep computations compared to a standard direct method. Finally, validations are made on plates and cylindrical geometries.

1. Introduction

Composite and plastic materials are now widely employed in a large variety of applications thanks to their light weight and good mechanical properties in particular for damping. In an other hand, the steel industry also brought innovative solutions to compete with these materials. Sandwich and laminated materials including viscoelastic materials are hence widely used in the transport domain such as automotive. The use of a viscoelastic layers is also widely spread in the glass industry, in particular for windscreens.

In order to predict the behavior of viscoelastic materials, a specific characterization is necessary. Indeed, their elastic moduli are complexes in order to take into account the elastic and viscous behaviors, but also frequency and temperature dependant as shown by Williams et al. [1] with the well known WLF law. The characterization is therefore made with a Dynamic Mechanical Thermal Analyzer (DMTA). Then the master curves obtained are generally approximated with polynomial functions but can also be parametrized with rheological models such as the Kelvin–Voigt model or the generalized Maxwell model.

To take fully advantage of viscoelastic damping properties, multilayered structures including viscoelastic materials must be used [2]. Indeed, the use of a Constrained Layer Damping (CLD) is very effective in sandwich structures thanks to the large deformation in the viscoelastic layer. Several studies have hence been undertaken on this subject since many years. The first equivalent model based on the effective bending stiffness was established by Ross et al. [3]. In this model, the properties of the multilayer are homogenized by considering only the shear deformation of the viscoelastic core. However, Rao [4] showed that the in-plane displacements across the thickness of each layer were not well describe in some cases, in particular for thick viscoelastic layers, and could have an influence on the calculated material damping. Douglas [5] and Sisemore and Darvennes [6] also showed that the compressional deformation in the core layer could have some important effects on the material damping. Finally, Xie and Shepard [7] proposed an enhanced analytical model and examined the relative contributions of each deformation to the structural damping.

In simple academic cases, analytical formulations can thus be employed in a similar way for different applications such as acoustics and active control of vibrations [8–10]. For complex geometries or complex boundary conditions that can be encountered in industrial configurations finite element models are still necessary. Each layer can then be modeled separately with 3D elements. However, the meshing and computational costs remain important with such models, and sometimes prohibitive. On the other hand, multilayered shell elements enable to reduce these costs. Among the possible shell models, one can distinguish the Equivalent Single Layer (ESL) and the Layer Wise (LW) models. The ESL models describe the displacements in all the layers with the same unknowns, while the LW models describe the displacements independently in

* Corresponding author.
E-mail address: jean-daniel.chazot@utc.fr (J.-D. Chazot).

0045-7949/$ - see front matter © 2011 Elsevier Ltd. All rights reserved.
doi:10.1016/j.compstruc.2011.05.015

each layer. An unified approach was also recently developed and used in multiphysics problems [11–13]. Among the LW models, the simplest are based on the first-order shear deformation theory (FSDT) [14,15] with linear displacements across the thickness of each layer. Then, the models based on the P-order shear deformation theory (PSDT) [16–18] enable to approximate the displacements across the thickness using a p-order polynom. Finally, a zigzag function can be added to describe more accurately the displacements at the interfaces between each layers [19–21]. In particular, when the elastic properties are very different in each layer, a high order approximation is necessary to model the in-plane and transverse displacements as shown by Cugnoni et al. in the PSDT model [16,17]. The zigzag function is then added to reduce the approximation order necessary with the previous PSDT model. The resulting ZPST model developed by Sulmoni et al. [20] is hence appropriated to model multilayered structures with viscoelastic layers.

When dealing with numerical models, the resolution method is very important. Here, due to the frequency dependance of the elastic moduli, the standard modal method cannot be employed to calculate a FRF. The direct frequency response method could be used instead. However, when the model size becomes important due to a high order of approximation, to a large mesh or for a dense frequency grid, the computational cost increases very fast. Specific numerical methods are then useful to deal with these problems. The iterative algorithm developed by Duigou et al. [22] enables for example to compute the complex modes and the structural damping of viscoelastic sandwich structures. An asymptotic numerical method has also been employed by Abdoun et al. [23] to compute the forced response of viscoelastic structures.

In the same way, methods based on Padé approximants have also been proposed to limit CPU time. Basically Padé approximant is the rational approximation of a function which agrees with its power series expansion to the highest possible order. The main advantage of Padé approximant is that convergence is not limited by poles contrary to the convergence of a power series expansion. This is a key point for the resonances dominated problems arising in acoustics and vibrations. The literature on this topic is plentiful and we restrict ourself to the references applying Padé approximant to finite element problems. Pinsky and coworkers [24], Malhotra and Pinsky [25] used the Padé via Lanczos approach to construct a reduced order model around a reference frequency with success. However the method is suitable only for particular frequency dependant matrices. Recently, Avery et al. [26] observed that the power series of the solution could be obtained quickly by the Liebnitz rule. They proposed thus an other approach for Padé approximant. This latter can be extended to iterative solver for large scale problem.

To sum up, in the present paper the ZPST element is used with viscoelastic materials. The frequency dependant elastic properties are taken into account with polynomial functions measured with a DMTA. The Padé method described by Avery et al. [26] is used to reconstruct the FRF, and experimental comparisons are made on these FRF.

2. Viscoelastic properties

Unlike steel or aluminium, viscoelastic materials are known to have frequency and temperature dependant elastic moduli. A frequency-temperature superposition principle exists (see Ref. [1]) and permits to obtain the master curves at a given temperature for a large frequency band by testing the material in a reduced frequency band at different temperatures.

A viscoelastic material sample is hence submitted to an harmonic strain $\varepsilon_{11}(\omega,T) = \underline{\varepsilon}_{11}e^{j\omega t}$ at a temperature T and a pulsation ω. The underbar refers to the magnitude of the variable that depends also implicitly on the temperature and the pulsation. The associated stress response $\sigma_{11}(\omega,T) = \underline{\sigma}_{11}e^{j(\omega t+\phi)}$ is dephased due to the viscous part of the material. The resulting relationship between strain and stress writes with a complex elastic modulus in order to take into account both the elastic and viscous behaviors of the material:

$$\sigma_{11}(\omega,T) = E^*(\omega,T)\varepsilon_{11}(\omega,T). \tag{1}$$

The real and imaginary parts of the complex Young's modulus E^* are respectively given by:

$$E'(\omega,T) = \frac{\underline{\sigma}_{11}}{\underline{\varepsilon}_{11}}\cos(\phi), \tag{2}$$

$$E''(\omega,T) = \frac{\underline{\sigma}_{11}}{\underline{\varepsilon}_{11}}\sin(\phi), \tag{3}$$

and the damping ratio can also be deduced from these equations as:

$$\eta = E''(\omega,T)/E'(\omega,T) = \tan(\phi). \tag{4}$$

The frequency-temperature superposition principle enables to obtain the master curves E' and E'' versus frequency at a given temperature by shifting all the measurements at the same temperature T_0 with a shift factor a_{T/T_0} such as:

$$\rho T E^*(\omega,T) = \rho_0 T_0 E^*(a_{T/T_0}\omega, T_0). \tag{5}$$

For polymer materials, the following WLF equation established by Williams et al. [1] is generally employed to determine the shift factor:

$$\log\left(a_{T/T_0}\right) = \frac{-C_1^0(T-T_0)}{C_2^0+T-T_0}. \tag{6}$$

The coefficients C_1^0 and C_2^0 used in this equation depend on the material and the temperature T_0. It is also important to note that the WLF Eq. (6) is only valid in the specific temperature range $T_g < T < T_g + 100$ °C above the glass transition temperature T_g.

The master curves are measured here with a Dynamic Mechanical Thermal Analyzer (DMTA). First, the coefficients C_1^0 and C_2^0 in Eq. (6) are identified with several measurements. Then all the measurements are shifted at the same temperature using the Eq. (5). Finally, the real and imaginary parts of the complex Young's modulus hence obtained are interpolated with polynoms such as:

$$E'(\omega,T) = \sum_{p=0}^{N} A_p\omega^p, \tag{7}$$

$$E''(\omega,T) = \sum_{p=0}^{N} B_p\omega^p. \tag{8}$$

In the following, three different materials widely used in the automotive industry have been tested. Fig. 1 presents their properties. Material A is quite soft and has good damping properties especially at low frequencies. Its damping ratio is greater than 0.09 below 100 Hz. Material B is the softest material and has the best damping properties on all the frequency band. Its damping ratio is always greater than 0.2. Material C is stiff and does not exhibit good damping properties. Its maximum damping ratio is 0.04 at 40 Hz. The polynomial fitting presented in Eqs. (7) and (8) is adapted to each case. For example, an order of 8 and 10 is sufficient to interpolate the real and imaginary part of the material C elastic modulus, while an order of 14 is necessary for the material B on two frequency bands. An order of 14 is also used for the material A on a single frequency band.

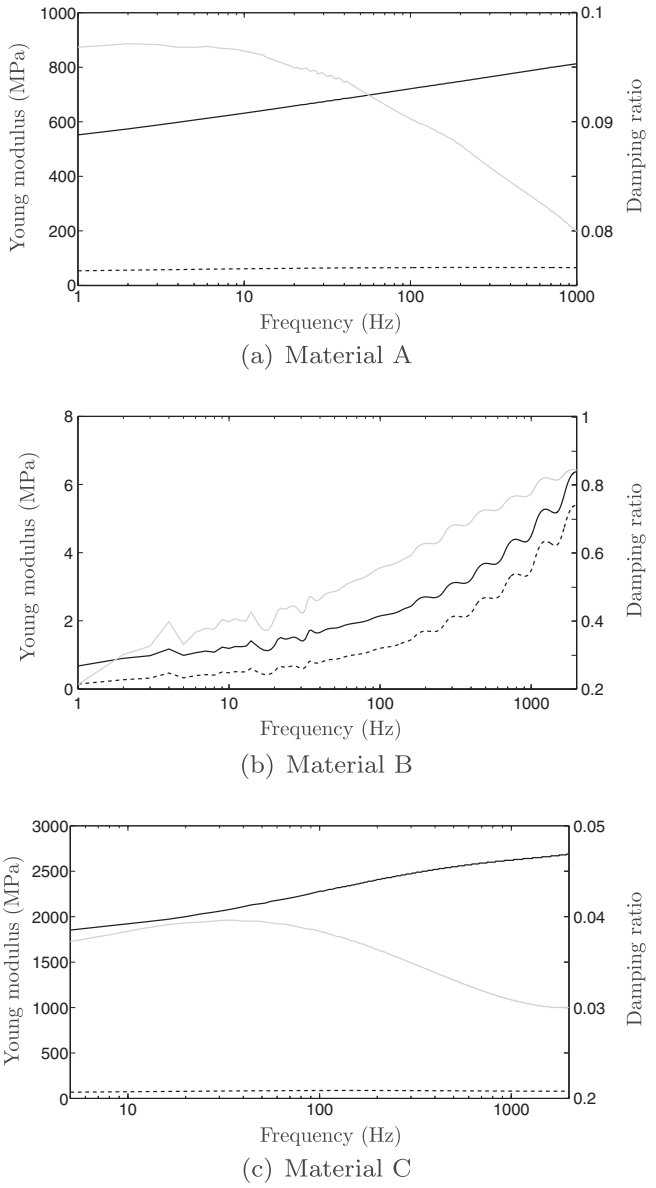

Fig. 1. Elastic properties – solid line: real part E' – dotted line: Imaginary part E'' – grey line: damping ratio η.

3. Finite element formulation

The forced vibration problem is described by the classical variational formulation:

$$\int_V \{\delta\boldsymbol{\varepsilon}\}^t \cdot \{\boldsymbol{\sigma}\} + \rho\{\delta\mathbf{u}\} \cdot \left\{\frac{\partial^2 \mathbf{u}}{\partial t^2}\right\} \mathrm{d}V = \int_V \mathbf{F_e} \cdot \delta\mathbf{u}\ \mathrm{d}V, \tag{9}$$

where $\boldsymbol{\varepsilon}$ and $\boldsymbol{\sigma}$ are the strain and stress tensors, $\mathbf{u}$ the displacement, ρ the density, and $\mathbf{F_e}$ the excitation force assumed to be harmonic in the following.

The finite element ZPST used in this paper is depicted in Fig. 2. The formulation presented in details by Sulmoni et al. [20] is reminded here briefly, and solved by FEM.

3.1. Displacement approximation

The displacement approximation employed in the ZPST element is depicted in Fig. 3 with the p-order approximation and the zigzag function. The zigzag function is added in order to enhance the convergence of the solution at the interfaces. The same approximation is used for the in-plane displacements along ξ_1 and ξ_2, and for the normal displacement along ξ_3.

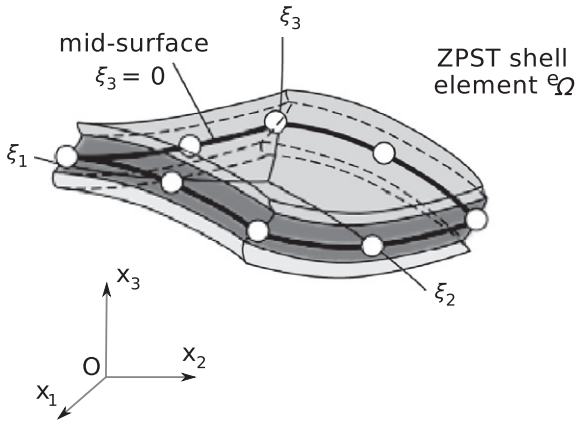

Fig. 2. ZPST shell element.

The displacement vector ${}^e\mathbf{u}$ over the element e is hence described with a p-order polynom and a first-order zigzag function such as:

$$\begin{aligned} {}^e\mathbf{u}(\boldsymbol{\xi}) = \sum_{i=1}^{n} H_i(\xi_1,\xi_2)\Big[{}^e\mathbf{q}_i^{(0)}(t) + \xi_3\,{}^e\mathbf{q}_i^{(1)}(t) + (-1)^K\zeta\,{}^e\mathbf{q}_i^{(Z)}(t) \\ + \frac{\xi_3^2\,{}^e\mathbf{q}_i^{(2)}(t)}{2!} + \cdots + \frac{\xi_3^p\,{}^e\mathbf{q}_i^{(p)}(t)}{p!}\Big], \end{aligned} \tag{10}$$

where $\boldsymbol{\xi} = \{\xi_1,\xi_2,\xi_3\}$ is the local coordinates vector, H_i is the ith shape function of the n-nodes quadratic shell element, $\mathbf{q}_i^{(j)}$ is the vector with the degrees of freedom of node i at the order j, $\mathbf{q}_i^{(Z)}$ is the vector with the degrees of freedom of node i corresponding to the zigzag function, K is the layer number and ζ is the transverse layer coordinate normalized between -1 and $+1$. Introducing t_k the thickness of the kth layer and t_t the total thickness of the multilayer, the relation between the local through-the-thickness coordinate ξ_3 and the transverse layer coordinate ζ writes then:

$$\xi_3 = -1 + 2\sum_{k=1}^{K-1}\frac{t_k}{t_t} + (1+\zeta)\frac{t_K}{t_t}. \tag{11}$$

Eq. (10) is then expressed in a reduced matrix form:

$${}^e\mathbf{u}(\boldsymbol{\xi}) = \mathbf{H}(\boldsymbol{\xi})\,{}^e\mathbf{q}, \tag{12}$$

where $\mathbf{H}(\boldsymbol{\xi})$ is the interpolation matrix over the n-nodes element such as $\mathbf{H}(\boldsymbol{\xi}) = [\mathbf{H}_1,\mathbf{H}_2,\ldots,\mathbf{H}_n]$, and $\mathbf{q}$ is the vector with all the degrees of freedom of the element such as ${}^e\mathbf{q} = \{{}^e\mathbf{q}_1,{}^e\mathbf{q}_2,\ldots,{}^e\mathbf{q}_n\}$. The shape functions of the ith node are hence collected in a matrix form such as:

$$\mathbf{H}_i = \begin{bmatrix} H_i & 0 & 0 & \xi_3 H_i & 0 & 0 & (-1)^K\zeta H_i & 0 & 0 \\ 0 & H_i & 0 & 0 & \xi_3 H_i & 0 & 0 & (-1)^K\zeta H_i & 0 \\ 0 & 0 & H_i & 0 & 0 & \xi_3 H_i & 0 & 0 & (-1)^K\zeta H_i \\ \ldots & \xi_3^p H_i/p! & 0 & 0 \\ \ldots & 0 & \xi_3^p H_i/p! & 0 \\ \ldots & 0 & 0 & \xi_3^p H_i/p! \end{bmatrix}.$$

3.2. Finite element discretization

The discretization with finite elements of the variational formulation (9) is then introduced and the interpolation matrix $\mathbf{H}$ is used

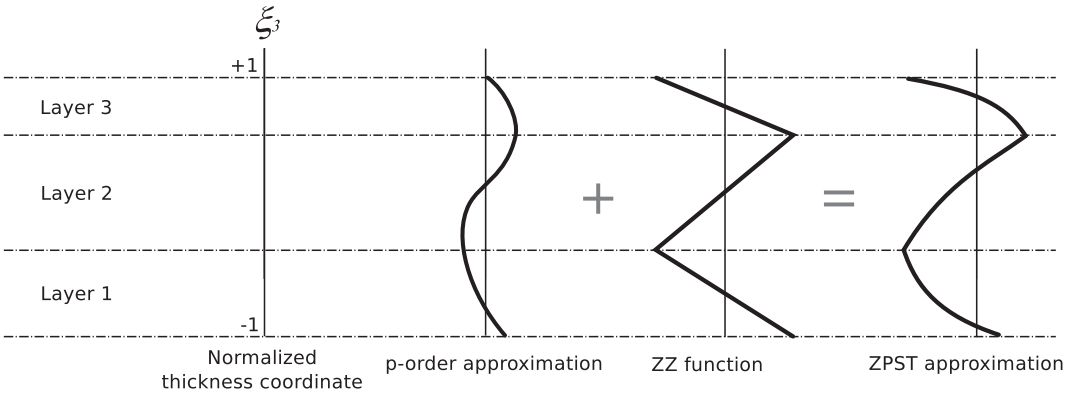

Fig. 3. ZPST displacement approximation.

to approximate the displacement over each element. The following elementary mass, stiffness, and force matrices are hence obtained:

$$ {}^e\mathbf{M} = \int_{eV} \rho \mathbf{H}^t \mathbf{H}\, dV, \quad {}^e\mathbf{K} = \int_{eV} {}^e\mathbf{B}^t {}^e\mathbf{C}\, {}^e\mathbf{B}\, dV, \quad {}^e\mathbf{F} = \int_{eV} \mathbf{H}^t \mathbf{F_e}\, dV, \quad (13) $$

where ${}^e\mathbf{B}$ refers to the strain–displacement matrix, while ${}^e\mathbf{C}$ refers to the strain–stress matrix. Being given that each element is made up of several layers with different properties, it is therefore necessary to integrate these matrices separately over each layer. Moreover the viscoelastic layer is characterized with a frequency dependant Young modulus. The resulting global strain–stress matrix ${}^e\mathbf{C}$ and stiffness matrix ${}^e\mathbf{K}$ are thus also frequency dependant.

Finally, the curved shell element is obtained from a master element. The integration over the curved element can be found in Ref. [20] with the details of the jacobian. A Gauss numerical integration is employed to calculate the elementary matrices.

The final global problem writes then by making the assembly of elementary matrices:

$$ (\mathbf{K}(\omega) - \omega^2 \mathbf{M})\mathbf{U} = \mathbf{F}, \quad (14) $$

where $\mathbf{K}(\omega)$ and $\mathbf{M}$ are the global stiffness and mass matrices, $\mathbf{U}$ is the generalized nodal displacement with all the degrees of freedom and $\mathbf{F}$ is the generalized nodal excitation. In this equation, $\mathbf{K}(\omega)$ and $\mathbf{M}$ are symmetrics.

4. The Padé reconstruction method

The frequency forced response computation of the mechanical system (14) is accelerated using Padé approximants. Instead of solving Eq. (14) at each frequency in a *fine* grid, the direct calculation is performed on a *coarser* grid (not necessarily regular) and the solution is reconstructed on the *fine* grid thanks to Padé approximant.

If U_d is the FEM solution at some dof d belonging to a dof subset $\mathcal{D}$, its power series expansion at ω_0 writes

$$ U_d(\omega_0 + \Delta\omega) = \sum_{i=0}^{\infty} u_i \Delta\omega^i, \quad (15) $$

with

$$ u_i = \frac{U_d^{(i)}(\omega_0)}{i!}. \quad (16) $$

Here, ω_0 is a sampling point on the *coarse* grid Ω. It is important to note that in many applications the response is only needed on a few nodes or a small dof subset $\mathcal{D}$ and not on all the meshing points. By definition, the U_d-Padé approximant $[L,M]$ is the rational fraction [27, Chapter 2]

$$ U_d(\omega_0 + \Delta\omega) = \frac{P(\Delta\omega)}{Q(\Delta\omega)} + O(\Delta\omega^{L+M+1}), \quad d \in \mathcal{D}, \quad (17) $$

which agrees with $L + M + 1$ first terms of the U_d power series expansion at ω_0. Here P is a polynom of degree L

$$ P = p_0 + p_1 \Delta\omega + \cdots + p_L (\Delta\omega)^L, \quad (18) $$

and Q is a polynom of degree M

$$ Q = q_0 + q_1 \Delta\omega + \cdots + q_M (\Delta\omega)^M, \quad (19) $$

with $q_0 = 1$. The polynoms P and Q have to be computed for each dof $d \in \mathcal{D}$ and for each value of $\omega_0 \in \Omega$.

The rational function used here enables to approximate more accurately the solution than the power series expansion. Indeed, for a solution with poles it is rather difficult to use a power series expansion to approximate the solution over a large frequency band while a rational function is more adapted in this case.

Padé coefficients calculation. To obtain the coefficients p_i and q_i, Eq. (17) is rewritten

$$ U_d(\omega_0 + \Delta\omega) Q(\Delta\omega) = P(\Delta\omega) + O(\Delta\omega^{M+L+1}). \quad (20) $$

Applying Liebnitz's rule on the derivative of a product [28, 3.3.8] with respect to $\Delta\omega$ yields [27, Chapter 2]

$$ \begin{pmatrix} u_{L-M+1} & u_{L-M+2} & \dots & u_L \\ u_{L-M+2} & u_{L-M+3} & \dots & u_{L+1} \\ \vdots & \vdots & & \vdots \\ u_L & u_{L+1} & \dots & u_{L+M+1} \end{pmatrix} \begin{pmatrix} q_M \\ q_{M-1} \\ \vdots \\ q_1 \end{pmatrix} = \begin{pmatrix} u_{L+1} \\ u_{L+2} \\ \vdots \\ u_{L+M} \end{pmatrix}, \quad (21) $$

and

$$ p_i = \sum_{k=0}^{i} q_k u_{k-i}, \quad (22) $$

with $u_i = 0$ if $i < 0$ by convention. First, the denominator coefficients q_i are the solution of Eq. (21). It is worth noting that this matrix is Toeplitz [27, Chapter 2] (or Hankel according the order of the unknowns) and can be inverted in $O(n^2)$ operations instead of $O(n^3)$ for arbitrary system of n linear equations. Nonetheless, a standard inversion is used in this paper. Even if the condition number is high, the q_i computation remains robust. Then numerators coefficients p_i are deduced from the denominators ones using Eq. (22). A prior condition is to compute the derivative of U_d at ω_0.

Derivatives calculation. First, the finite element impedance matrix is introduced

$$ \mathbf{Z}(\omega) = \mathbf{K}(\omega) - \omega^2 \mathbf{M}. \quad (23) $$

The global problem given in Eq. (14) writes now

Table 1
Example of computational times with 1 central frequency f_0 and 25 intermediate frequencies f_i taken into account. Results are computed on 1 element with 120 dof. Calculations are made with Matlab on an Intel (R) Xeon (R) CPU E5430 @ 2.66 GHz, 16Go RAM (see [32]).

	CPU time (s) f_0	CPU time (s) f_i	CPU time (s) 1 f_0, 25 f_i	Speed up
20295 dofs				
Direct method	62	62	1550	
Padé with 6 derivatives	72	1.4	107	14
Padé with 10 derivatives	87	1.7	129	12
Padé with 14 derivatives	108	2.2	163	10
90585 dofs				
Direct method	228	228	5700	
Padé with 6 derivatives	274	1.9	321	18
Padé with 10 derivatives	346	3.1	423	13
Padé with 14 derivatives	436	4.1	538	11

Table 2
Characteristics of each material.

Material	E (Pa)	η(%)	ν	ρ (kg/m^3)
Steel 1	2.04e11	0.16	0.30	7680
Steel 2	2.10e11	0.10	0.30	7850
Material A	Fig. 1	Fig. 1	0.49	950.0
Material B	Fig. 1	Fig. 1	0.45	1139
Material C	Fig. 1	Fig. 1	0.30	967.0

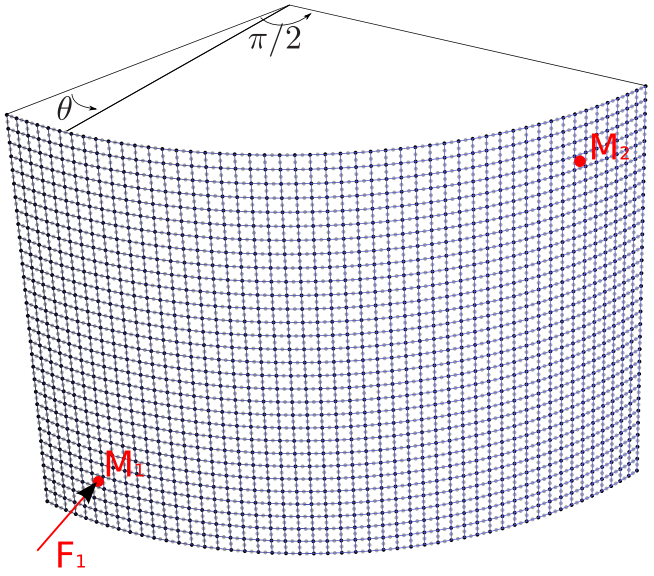

Fig. 4. 2D mesh used for the curved laminated shell.

$$\mathbf{Z}(\omega)\mathbf{U} = \mathbf{F}(\omega). \tag{24}$$

Applying again Liebnitz's rule for the derivative of a product and putting $\omega = \omega_0$ yields

$$\mathbf{Z}_0\mathbf{U}_0^{(k)} = \mathbf{F}_0^{(k)} - \sum_{r=0}^{k-1} \frac{k!}{r!(k-r)!}\mathbf{Z}_0^{(k-r)}\mathbf{U}_0^{(r)}, \quad k = 0, 1, 2, \ldots, L+M+1, \tag{25}$$

where '0' subscript denotes the functions are evaluated at $\omega = \omega_0$. Thanks to Eq. (25) all derivatives of U_d can be obtained by a simple iterative process which requires (i) the factorization of the matrix $\mathbf{Z}_0$ (stated later); (ii) the derivatives of $\mathbf{Z}_0$ and of $\mathbf{F}_0$.

To calculate these derivatives, the stiffness matrix is splitted into two parts

$$\mathbf{Z} = \mathbf{K}_0 + E^*(\omega)\mathbf{K}_1 - \omega^2\mathbf{M}. \tag{26}$$

Here the matrices $\mathbf{K}_0$ related to the elastic layers and $\mathbf{K}_1$ related to the viscoelastic layer are now independent of frequency. The derivatives $\mathbf{Z}_0^{(k-r)}$ are thus straightforward because $E^*(\omega)$ is a simple polynom (see Eqs. (7) and (8)). It is also important to note that the assembly of FE matrices is only performed once.

Matrix factorization. The factorization is carried out thanks to LU factorization [29,30] because multiple RHS can be easily solved once the factorization is achieved. A drawback of Padé methods is that the storage of L and U matrices is required. However if a reordering algorithm (nearly indispensable) such AMD [31] is applied to reduce the fill-in in the matrices L and U, these matrices remain sparse and the storage is not a real problem for the applications proposed here. The other approach proposed by Avery et al. and using an iterative solver is detailed in [26] and may be suitable for large scale problems.

Computational aspect. In the following of the paper we will consider only the case where the polynomial P and Q have the same order ($M = L$) for sake of simplicity. In all the performed simulations this assumption leads to accurate results. Two parameters can also be adjusted to enhance the quality of the reconstruction:

- The number of frequency points on the *coarse* grid. If there are not enough points, the approximation may be not accurate between two points. Simple linear meshing has been performed for Ω and is sufficient at low frequencies. At higher frequencies it is suitable to follow roughly the modal density of the system. Through numerical tests, it has been shown that taking more or less as many points as poles in the studied frequency band is a good rule. However, this is not a stringent assumption because, once the coarse grid approximation has been computed, a simple comparison of the reconstructed fields between two sampling points (see Fig. 6(b)) leads to an efficient convergence test. Then, it is possible to add frequency points one by one, by dichotomy, until a convergence criterion is reached.
- *The number of derivatives*. The accuracy of the reconstructed solution depends on the number of derivatives. However, the condition number in Eq. (21) depends also on this number. In practice, the number of derivatives that gives a good compromise between the accuracy and the conditioning number is found between 5 and 10. An example on the effect of the number of derivatives is presented in Section 5.1.

If too many points or too many derivatives are chosen, the efficiency in computational time will not be optimal. It is therefore important to adjust these parameters carefully.

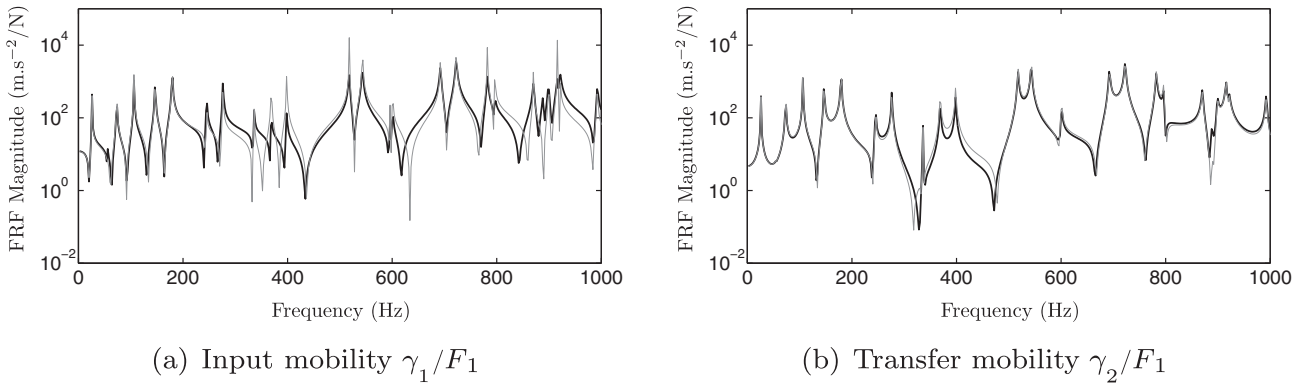

Fig. 5. FRF comparison for the curved laminated shell – black lines: 3D model – grey lines: ZPST model.

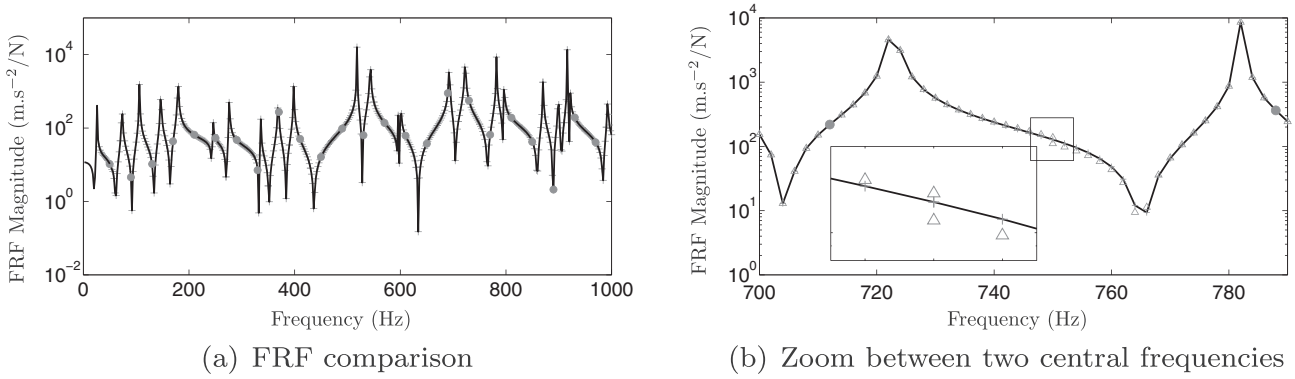

Fig. 6. FRF comparison for the curved laminated shell with the ZPST model on FRF γ_1/F_1 – black line: ZPST model without approximation – + : Padé approximation with 6 derivatives – △: Padé approximation with 10 derivatives – • : central frequencies.

Finally the global resolution algorithm is the following:

Algorithm 1. Padé approximant

1: Build the matrix **M**, $\mathbf{K}_0$, $\mathbf{K}_1$
2: **for** $\omega_0 \in \Omega$ **do**
3: Build the matrices $\mathbf{Z}_0$
4: Compute the matrix $\mathbf{Z}_0$ factorisation
5: Compute the k-first derivatives of **U** by solving (25)
6: **for** $d \in \mathcal{D}$ **do**
7: Compute **q** and **p**
8: Compute U_d in the bandwidth
9: Check convergence
10: **end for**
11: **end for**

Obviously, the smaller is the number of dof $\mathcal{D}$ to reconstruct, the faster is the computation, but in practice the reconstruction step 6 is very fast in comparison with step 5. An example of CPU time is presented in Table 1 for 20,295 and 90,585 dof. One central frequency is taken into account with 25 intermediate frequencies. The solution is reconstructed over 1 element with 120 dof. Finally, the ratio of the CPU time between the direct method and the Padé approximation method gives a speed up always greater than 10.

5. Results and validations

In order to validate the present methodology and to illustrate its potential, results on two benchmark configurations are presented

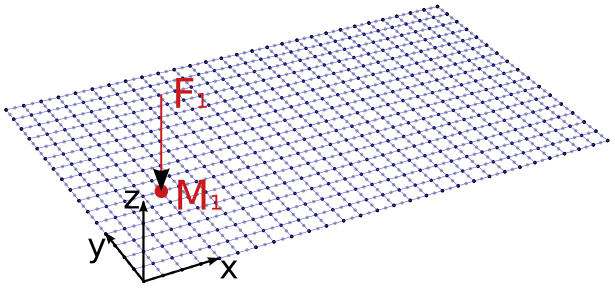

Fig. 7. Mesh 28 × 16 used for the sandwich plate 1.

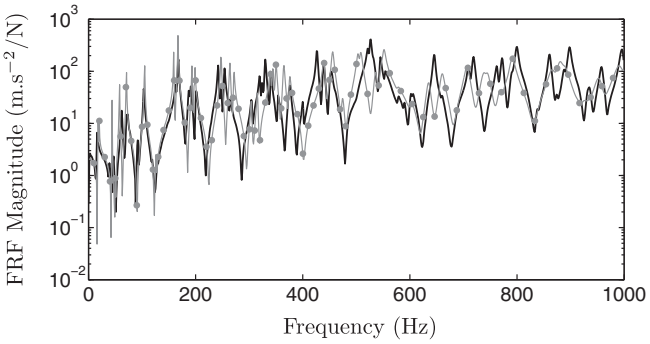

Fig. 8. Input mobility γ_1/F_1 comparison for the sandwich plate – thick black line: experiment-thin grey line: ZPST model with 10 derivatives – • : central frequencies.

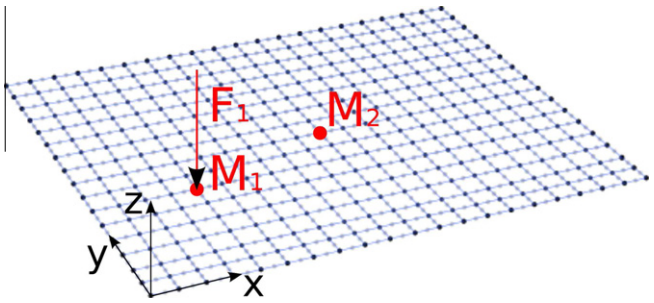

Fig. 9. Mesh 20 × 16 used for the sandwich plate 2.

and compared respectively with a 3D finite element model and the experiment : (i) a curved laminated shell and (ii) a sandwich plate. The calculation parameters used in all the simulations that follow are detailed below.

The materials used in the following are presented in Table 2. Quadratic quadrangles Q8 are used in the ZPST model. The order ($p = 3$) for the displacement approximation, the number of central values and of derivatives in the Padé approximant reconstruction method, and the mesh refinement have been chosen to ensure the convergence of the model.

5.1. Curved laminated shell

The viscoelastic shell element is compared here with a 3D finite element on a curved geometry to evaluate its efficiency. The reference 3D mesh is made of 3000 quadratic hexahedral elements ($30 \times 50 \times 2$) and an exact integration is done with Gauss points. The tested multilayered sample is a quarter of a cylinder with two layers of dimensions $R = 0.2$ m and $H = 0.2$ m. The exterior layer is made of steel 1 and has a thickness of 0.5 mm. The viscoelastic interior layer is made of material C and has a thickness of 0.3 mm. Two points are used to identify input and transfer mobilities: $M_1(\theta = \pi/8; H = 0.025$ m), and $M_2(\theta = 7\pi/8; H = 0.175$ m). Free boundary conditions are applied in both models, and the 2D mesh used in this comparison is presented in Fig. 4.

Input and transfer mobilities for the curved laminated shell are compared with the two models in Fig. 5. In this case, the direct method is used in order to compare first the models without the specific numerical method. The results obtained with the ZPST model are in good agreement with the 3D model over the whole frequency band. The slight differences observed in the results are explained by the differences in the geometry with a 2D model and a 3D model. In spite of the viscoelastic layer, the resonances are still visible on the whole frequency band. The viscoelastic layer is however not constrained between two skins. Its efficiency to damp the system is therefore reduced.

On Fig. 6(a) is presented a comparison between the Padé approximant method with 25 central frequencies and 14 derivatives and the direct method. Both FRF are indiscernible and the accuracy of the Padé approximant method is hence demonstrated. However, the number of central frequencies, and the number of derivatives must be taken carefully to obtain the convergence of the Padé approximation.

The effect of the number of derivatives in the Padé approximation is presented in Fig. 6(b). At the junction between two central frequencies, a discontinuity is noticed with six derivatives. This discontinuity is smoothed when 10 derivatives are used. It is also worthwhile to notice that the number of derivatives depends on the variations of the response. For smooth variations, the number of derivatives is limited (e.g. highly damped system or far from the peaks). On the contrary, if the variations are important, it is necessary to increase the number of derivatives. In practice a number of derivatives between 5 and 10 yields to an acceptable reconstruction error for engineering application.

5.2. Sandwich plates

Two sandwich plates are considered here. Free boundary conditions are applied in the experiment and in the model. The panels are suspended with two soft strings and excited with a hammer. Accelerations are then measured at observation points with accelerometers.

5.2.1. Sandwich plate 1

The first multilayered sample tested is a plane sandwich plate of dimensions 0.7 m by 0.4 m. The skins are two identical plates of steel 2 and have a thickness of 0.25 mm. The viscoelastic core is made of material A and has a thickness of 0.8 mm. The input mobility is measured at point $M_1(0.1$ m; 0.15 m). The 28×16 mesh used is presented in Fig. 7.

An input mobility comparison between the model and the experiment is presented in Fig. 8. At low frequency, the results obtained with the ZPST model are in good agreement with the measurements. It is important to say that no tuning was made on the numerical results (i.e. the viscoelastic properties in the computation are measured with a DMTA). Above 400 Hz, slight differences are noted but the global trend is still correct. These differences can be explained by measurement uncertainties in the characterization of the viscoelastic material properties. The making process can also modify the material properties at the interface. For thinner viscoelastic layers, this interface effect can be even more important.

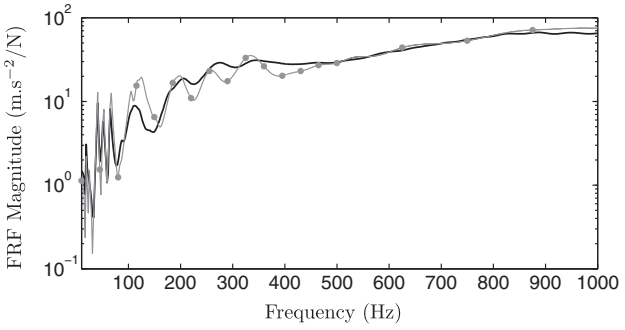

(a) Input mobility γ_1/F_1

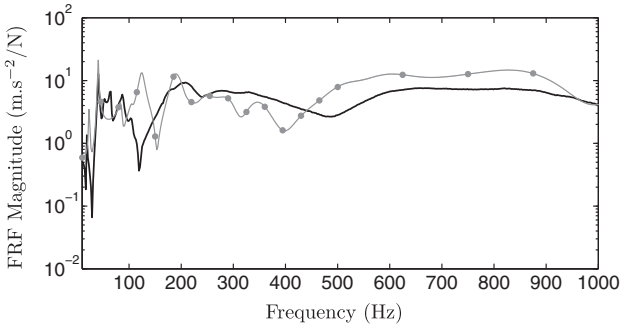

(b) Transfer mobility γ_2/F_1

Fig. 10. FRF for the sandwich plate 2 – thick black lines: experiment – thin grey lines: ZPST model with 10 derivatives – •: central frequencies.

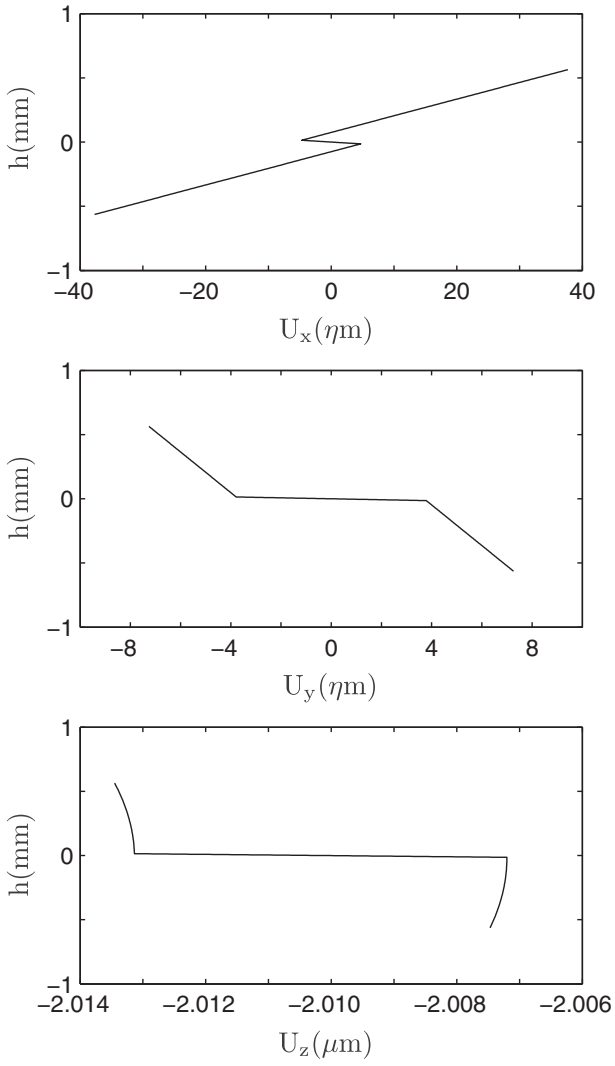

Fig. 11. Displacements fields at 200 Hz at point M_1 for the sandwich plate 2 excited by a unit force F_1.

5.2.2. Sandwich plate 2

The second multilayered sample tested is a sandwich plate of dimensions 0.5 m by 0.39 m. The skins are two identical plates of steel 1 and have a thickness of 0.55 mm. The viscoelastic core is made of material B and has a thickness of 28 μm. The input and transfer mobilities are measured at two points: M_1(0.1 m; 0.15 m), and M_2(0.25 m; 0.2 m). Finally, the 20×16 mesh used is presented in Fig. 9.

A comparison of input and transfer mobilities for the sandwich plate 2 between the model and the experiment is presented on Fig. 10. Once again, no tuning is made on the numerical model. At low frequency, the results obtained with the ZPST model are still in good agreement with the measurements. However, contrary to the previous comparison, above 100 Hz large differences appear. We also found the same results with a 3D finite element model. Therefore, the differences do not come from the model but rather from the interface effect. Indeed, the viscoelastic layer is very soft and very thin. The gluing process adds thus an interface that is not negligible and that changes the viscoelastic layer characteristics.

In order to illustrate the phenomenons at the interface with the thin viscoelastic layer, the displacements fields along the three directions at the point M_1 are depicted in Fig. 11. An harmonic excitation of 200 Hz is applied at the same point. The importance of the ZZ function in the approximation is clearly demonstrated here in the case of a very thin core much softer than the skins. A sharp variation in the displacement at the interface with the viscoelastic core is indeed visible for each component. This behavior shows that the viscoelastic layer is preponderant on the global response of the structure. Therefore, the interface effect related to the gluing process cannot be neglected here. It explains also the differences obtained between the model and the experiment.

6. Conclusions and prospects

The efficiency of the ZPST shell element to model viscoelastic curved structures has been demonstrated in this paper with two main advantages : to reduce the meshing time and to reduce the computational time. Frequency dependant material properties have hence been taken into account for the viscoelastic layers. The Padé approximant method has also been used to evaluate the frequency response functions. Finally, some problems have been highlighted for very thin viscoelastic layers. Indeed, the material properties identified with a DMTA can be modified by the making process at the interface of thin viscoelastic layers. Work is on going on identification of viscoelastic properties of thin cores in sandwich structures.

Acknowledgements

The authors acknowledge the project MAEVA and their industrial partners in this project: ESI Group, Vibratec, and Arcelor-Mittal. The authors acknowledge also the Project Pluri-Formations PILCAM2 at the Université de Technologie de Compiègne for providing HPC resources that have contributed to the research results reported within [32].

References

[1] Williams M, Landel R, Ferry J. The temperature dependence of relaxation mechanisms in amorphous polymers and other glass-forming liquids. J Am Chem Soc 1955;77:3701–6.
[2] Jones DIG. Reflections on damping technology at the end of the 20th century. J Sound Vib 1996;190(3):449–62.
[3] Ross D, Ungar E, Kerwin Jr E. Damping of plate flexural vibrations by means of viscoelastic laminate. Struct Damping (ASME) 1959:49–88.
[4] Rao D. Vibration of short sandwich beams. J Sound Vib 1977;52:253–63.
[5] Douglas B. Compressional damping in three-layer beams incorporating nearly incompressible viscoelastic cores. J Sound Vib 1986;104:343–7.
[6] Sisemore C, Darvennes C. Transverse vibration of elastic–viscoelastic–elastic sandwich beams: compression-experimental and analytical study. J Sound Vib 2002;252:155–67.
[7] Xie Z, Shepard Jr S. An enhanced beam model for constrained layer damping and a parameter study of damping contribution. J Sound Vib 2009;319(3–5):1271–84.
[8] Guyader J, Lesueur C. Transmission of reverberant sound through orthotropic, viscoelastic multilayered plates. J Sound Vib 1980;70(3):319–32.
[9] Ghinet S, Atalla N, Osman H. The transmission loss of curved laminates and sandwich composite panels. J Acoust Soc Am 2005;118(2):774–90.
[10] Trindade MA, Benjeddou A, Ohayon R. Finite element modelling of hybrid active–passive vibration damping of multilayer piezoelectric sandwich beams – Part I: Formulation. Int J Numer Methods Eng 2001;51(7):835–54.
[11] Brischetto S, Carrera E. Coupled thermo-mechanical analysis of one-layered and multilayered plates. Compos Struct 2010;92(8):1793–812.
[12] Carrera E, Nali P. Multilayered plate elements for the analysis of multifield problems. Finite Elem Anal Des 2010;46(9):732–42.
[13] Carrera E, Brischetto S, Cinefra M. Variable kinematics and advanced variational statements for free vibrations analysis of piezoelectric plates and shells. Comput Model Eng Sci 2010;65:259–342.
[14] Kärger L, Wetzel A, Rolfes R, Rohwer K. A three-layered sandwich element with improved transverse shear stiffness and stresses based on FSDT. Comput Struct 2006;84(13–14):843–54.
[15] Amichi K, Atalla N. A new 3d finite element for sandwich beams with a viscoelastic core. J Vib Acoust 2009;131(2):1–9.
[16] Cugnoni J, Gmür T, Schorderet A. Modal validation of a set of c0-compatible composite shell finite elements. Compos Sci Technol 2004;64(13–14):2039–50.
[17] Cugnoni J, Gmür T, Schorderet A. Identification by modal analysis of composite structures modelled with FSDT and HSDT laminated shell finite elements. Compos Part A: Appl Sci Manuf 2004;35(7–8):977–87.

[18] Matter M, Gmür T, Cugnoni J, Schorderet A. A PSDT shell finite element formulation including structural damping. Comput Struct 2010;88(15–16):902–8.
[19] Carrera E. Historical review of zig-zag theories for multilayered plates and shells. Appl Mech Rev 2003;56(3):287–308.
[20] Sulmoni M, Gmür T, Cugnoni J, Matter M. Modal validation of sandwich shell finite elements based on a p-order shear deformation theory including zigzag terms. Int J Numer Methods Eng 2008;75:1301–19.
[21] Fares M, Elmarghany M. A refined zigzag nonlinear first-order shear deformation theory of composite laminated plates. Compos Struct 2008;82(1):71–83.
[22] Duigou L, Daya EM, Potier-Ferry M. Iterative algorithms for non-linear eigenvalue problems. Application to vibrations of viscoelastic shells. Comput Methods Appl Mech Eng 2003;192(11–12):1323–35.
[23] Abdoun F, Azrar L, Daya EM, Potier-Ferry M. Forced harmonic response of viscoelastic structures by an asymptotic numerical method. Comput Struct 2009;87(1–2):91–100.
[24] Wagner MM, Pinsky PM, Malhotra M. Application of padé via lanczos approximations for efficient multifrequency solution of helmholtz problems. J Acoust Soc Am 2003;113(1):313–9.
[25] Malhotra M, Pinsky PM. Efficient computation of multi-frequency far-field solutions of the helmholtz equation using padé approximation. J Comput Acoust 2000;8(1):223–40.
[26] Avery P, Farhat C, Reese G. Fast frequency sweep computations using a multi-point padé-based reconstruction method and an efficient iterative solver. Int J Numer Methods Eng 2007;69(13):2848–75.
[27] Graves-Morris PR, Baker GAJ. Padé approximants, encyclopedia of mathematics. Addison Wesley: Cambridge University Press; 1981.
[28] Abramowitz A, Stegum I. Handbook of mathematical functions. New York: Dover Publ.; 1965.
[29] Davis TA. Algorithm 832: Umfpack, an unsymmetric-pattern multifrontal method. ACM Trans Math Soft 2004;30(2):196–9.
[30] Amestoy PR, Duff IS, L'Excellent J-Y. Multifrontal parallel distributed symmetric and unsymmetric solvers. Comput Methods Appl Mech Eng 2000;184:501–20.
[31] Amestoy PR, Davis TA, Duff IS. Algorithm 837: Amd, an approximate minimum degree ordering algorithm. ACM Trans Math Soft 2004;30(3):381–8.
[32] <http://pilcam2.wikispaces.com>.